Fracture Resistance and Crack Growth Mechanisms in Functionally Graded Ti–TiB

G. SAHRAGARD-MONFARED, C.M. SMUDDE, R.D. CARPENTER, Z.A. MUNIR, and J.C. GIBELING

This paper presents the results of fracture tests and crack path observations for a layered functionally graded material (FGM) consisting of Ti and TiB phases. The composition varied in a nearly linear manner from a TiB-rich layer at the bottom to commercially pure (CP) Ti at the top. Elastic properties of the mixed phase interlayers were measured using nanoindentation testing, demonstrating a linear variation with composition. These results differ significantly from approximations calculated in previous studies using a non-linear rule-of-mixtures approach. Fracture tests were conducted on single edge notch bend [SEN(B)] specimens with the notch aligned orthogonal to the direction of the composition gradient. For this crack orientation, "average" R-curve behavior based on the J-integral was investigated to understand the mechanics of crack growth. The value of J was found to be minimal (less than 1 N/mm) below 47 pct volume fraction of TiB compared to a reported value of approximately 150 N/mm for pure Ti. These results indicate that a steeper transition to high concentrations of the metallic phase is necessary to achieve adequate fracture resistance in this metal/ceramic FGM. Observations on the specimen surface indicate crack path toughening mechanisms of this functionally graded material include crack bridging, branching, and deflection.

I. INTRODUCTION

METAL/CERAMIC functionally graded materials (FGMs) were originally developed to create materials that could survive in high-temperature environments and still have acceptable crack propagation resistance by reducing the thermally induced stresses below the fracture strength of the ceramic.[1] To minimize residual stresses, it was proposed to gradually vary the composition from metal to ceramic. This approach takes advantage of the desirable characteristics of the constituent components (e.g., high hardness and thermal resistance on one side and high toughness on the other) and enables the fabrication of the FGM with minimal residual stress that might cause interlayer cracking. The FGM composition can be varied either continuously or in a layered (discontinuous) manner, although the latter is generally simpler. In this approach, the layers can be made thinner and the composition varied in smaller steps until the residual thermal stresses are accommodated. Throughout the 1980s and 90s, FGMs were produced by a number of methods including chemical vapor deposition,[2] metal powder sintering,[3] high-temperature plasma spraying,[4] self-propagating combustion synthesis (SHS),[5,6] thermo-chemical diffusion, sedimentation of slurried powders,[7] and X-ray degradation of a plastic co-polymer.[8]

In the past decade, advances in additive manufacturing (AM) have led to renewed interest in FGMs, as AM opens new opportunities for producing them. In fact, the layer-by-layer deposition process of AM offers a distinctive advantage to produce parts with compositions and properties that vary spatially in three dimensions. Dozens of papers on AM of FGMs have been written in recent years and much of the primary literature on this topic is summarized in several recent comprehensive reviews.[9–12] As described in these reviews, AM has been applied to a variety of metal-metal systems (e.g., the joining of ferritic and austenitic steels or stainless steel to nickel-based alloys) as a way to join dissimilar metals with a composition gradient that overcomes the disadvantages of conventional welding or mechanical fastening. Additive manufacturing has also been used to fabricate a variety of metal/ceramic FGMs, such as Ti6Al4V/TiC and Ti6Al4V/Al_2O_3.[12] The primary AM method used to build FGMs is directed

G. SAHRAGARD-MONFARED, C. M. SMUDDE, R. D. CARPENTER, Z. A. MUNIR, and J. C. GIBELING are with the Department of Materials Science and Engineering, University of California, One Shields Avenue, Davis, California 95616. Contact e-mail: jcgibeling@ucdavis.edu
R. D. Carpenter—Deceased.

energy deposition (DED) using multiple hoppers of source powders.[9,10] Alternatively, selective laser melting of FGMs has proven effective, typically using pre-mixed powders of the desired compositions.[11,12]

Many of the studies of AM of FGMs have focused on proof-of-concept, understanding the phases that form, developing strategies to avoid undesirable phases such as brittle intermetallics, and identifying the number and compositions of layers needed to successfully build a discontinuous FGM. Some authors have measured the mechanical properties of the resultant builds such as hardness, strength, and ductility.[9–12] However, even after many years of interest, there are very few experimental studies of the fracture behavior of FGMs produced by AM or any other method.[13,14]

In metal/ceramic FGMs, cracks propagating from the ceramic side to the metal side should be impeded by the increasing toughness through the FGM (resulting in rising R-curve behavior). Consistent with this expectation, Jin and Batra first theoretically predicted rising R-curve behavior for metal/ceramic FGMs.[15] They subsequently described the theoretical R-curve and strength behavior of a metal/ceramic FGM based on specimen size, loading conditions and metal particle size.[16] They used a rule of mixtures for the Young's modulus, shear modulus, and Poisson's ratio and noted that "the micro-mechanical models developed for macro-homogeneous composites are only approximately valid for FGMs".[16] Later work by Shim, et al. verified that a modified boundary layer model could be used to predict rising R-curve behavior in FGMs.[17]

The limited experimental fracture results are a consequence of the small size of FGMs commonly produced. Miller, et al. determined the fracture strength of small beams in four-point bending.[18] To overcome the size limitation, Tomsia, et al. reported fracture toughness of Mo/mullite FGMs based on cracks at the corners of Vickers micro-hardness indentations.[7] Using larger fracture specimens similar to those tested in the present work, Hill, et al. experimentally investigated the stress intensity factor of a Ti–TiB FGM during fracture testing.[14] However, these studies assumed linear elastic fracture behavior which may not be accurate for FGMs since increasing plasticity is expected as the crack propagates into the metal-rich layers. In other previous work, the elastic and plastic components of the fracture

resistance were determined for a single experimental J-integral curve for the Ti–TiB FGM, although the reported values are in error as noted below.[19] Due to the limited number of fracture experiments on metal/ceramics FGMs, there is no detailed published information describing the interaction of a crack tip with the different microstructural features present at various positions within the material. Hence, understanding of the toughening mechanisms is very limited.

The goal of the current research is to present a new understanding of the mechanisms and mechanics of crack propagation in metal/ceramic FGMs to support evolving efforts in AM to produce these promising materials. The mechanisms of crack propagation are explored by examining the crack path to determine the processes that were active as the crack tip interacted with different phases present in each layer. Previous studies of the Ti–TiB FGM described in this work have not examined these crack tip damage and toughening processes. The mechanics of crack propagation are characterized using elastic–plastic fracture mechanics applied to multiple single edge notched bend [SEN(B)] specimens tested in three-point bending. The observations presented in this work also provide important guidance for the design of more fracture resistant metal/ceramic FGMs that could be realized by additive manufacturing.

II. MATERIALS PROCESSING AND EXPERIMENTAL PROCEDURES

The material studied in this investigation was a seven-layered functionally graded titanium-titanium monoboride (Ti–TiB) laminate prepared using a commercially pure (CP) Ti plate and tape cast mixtures of titanium and titanium diboride (TiB_2) powders. Details of the powder composition, manufacturing process, and the resulting plate are described elsewhere[14,19–21] and the layer compositions are listed in Table I. All phase fractions are expressed by volume in the present work. As demonstrated by Sahay, et al., solid-state processing of Ti and TiB_2 results in the formation of TiB with very little residual TiB_2 in the finished FGM.[21] The final FGM plate was a square of 150 mm on each side and a thickness of approximately 17 mm.

Table I. Summary of Material Property Data for 7-Layered Ti–TiB FGM

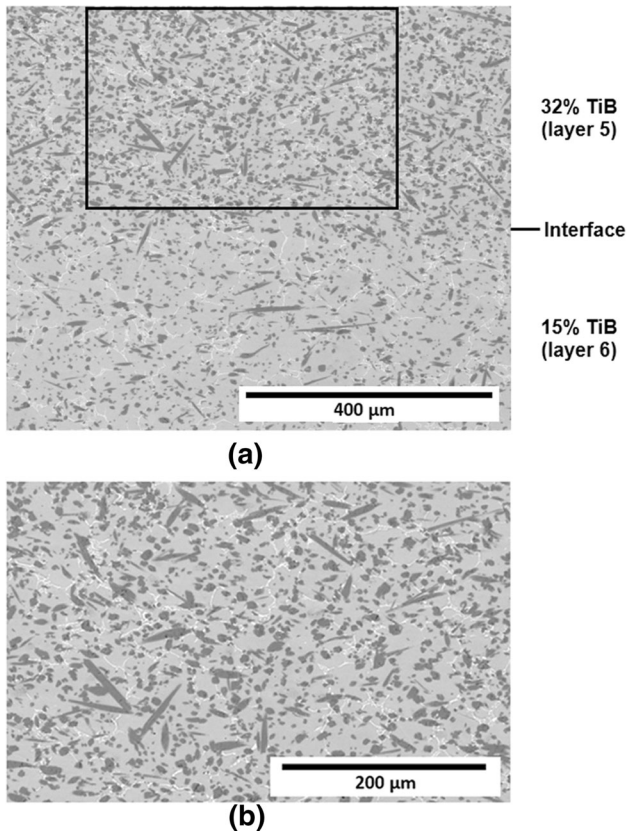| Layer	Composition Pct Ti	Composition Pct TiB	Nominal Thickness (mm)	E (GPa) Expt.	E (GPa) Modified RoM	v Equation [1]
—	0	100	—	—	408 [20]	0.16 [31]
1	15	85	2.5	392 ± 15	301	0.19
2	21	79	1.7	377 ± 21	272	0.2
3	38	62	1.8	295 ± 26	214	0.23
4	53	47	1.4	233 ± 24	180	0.26
5	68	32	1.8	184 ± 20	155	0.29
6	85	15	2.1	152 ± 8	134	0.32
7-CP Ti	100	0	3.4	135 ± 3	119 [20]	0.35 [31]

Fig. 1—(a) Backscattered electron image of the interface between layers 5 and 6 illustrating the interfacial integrity in this Ti–TiB FGM. (b) SEM image of Ti–TiB FGM layer 5 (32 pct TiB) from the black box in (a). In these images the TiB particles (dark gray) are distributed in a Ti matrix (gray) with a discontinuous grain boundary network of NiTi (white).

Microscopy specimens were polished on nylon cloth with 6 and 1 μm diamond paste and a final polish with alumina on flocked cloth. The specimens were examined using a scanning electron microscope (SEM) operating in backscatter mode. As previously observed by others, the TiB particles exhibited two distinct morphologies: blocky and needle shaped as revealed in Figure 1, which shows the boundary of layers 5 and 6 and a zoomed in section of the fifth layer in the FGM containing 68 pct Ti and 32 pct TiB.[21–24] The boundary shown in Figure 1 illustrates complete layer bonding and lack of interfacial defects in this FGM. Also shown in Figure 1 is the discontinuous grain boundary network NiTi from the proprietary sintering aid material. A similar result was observed by Sahay, et al. in the same material.[21]

Single edge notched bend [SEN(B)] specimens were cut from the plate using electro-discharge machining with the machined notch on the side containing the highest concentration of TiB as illustrated in previous work.[19] Specimens were machined to widths (W) in the range 13.8 to 14.9 mm (due to the varying thickness of the hot-pressed plate), a thickness (B) of 7.37 mm and a length of 79.38 mm, with a notch 5.08 mm deep ($a_o/W = 0.345$) including integral clip gage knife edges in accordance with ASTM E1820-20. The machined crack mouth opening displacement (CMOD) gage length was 6.35 mm. CMOD was measured using an MTS Model 632.03E–30 clip gage. The fracture experiments were conducted in three-point bending at room temperature on an MTS 810 servohydraulic load frame running MTS TestStar II control software.

Prior to conducting the fracture experiments, pre-cracking of specimens FGM 4 and FGM 6 by reverse 4-point bending fatigue was used to successfully create a controlled, short, sharp precrack at the machined notch of 0.01 to 0.1 mm, suitable for accurate measurement of the J–R experiments.[19] However, these were slightly smaller than the target precrack length of 0.2 mm from the starting notch which would have given the desired initial crack size (a_o) of $a_o/W = 0.358$ for the fracture experiments. The precracked specimens were heat tinted at 400 °C for 60 minutes to mark the size and shape of the actual starting crack. This relatively low temperature is not expected to alter the phase composition of the material. A third specimen (FGM 5a) was not pre-cracked, however, upon initial loading the crack popped in to 7.53 mm. Data analysis for specimen FGM 5a began at the point of pop-in, essentially treating the pop-in as a precrack.

It was initially believed that experimental results obtained from J-integral testing as described in ASTM Standard E1820 would most accurately represent the FGM material because nonlinear plastic deformation was expected in the metal-rich layers of the FGM and inclusion of the plastic portion of the J-integral would account for this deformation. Therefore, fracture testing to determine the J–R response of the specimens was conducted in three-point bending according to ASTM E1820-20 as described previously.[14,25] The force was increased by the amount necessary to increase the crack mouth opening displacement by at least 0.00254 mm. After each such increment, the specimens were held for thirty seconds to permit relaxation of any time dependent crack extension and allow stable crack growth to occur.

Because layered FGMs are anisotropic and the elastic modulus varies with location in the layers, the typical compliance method could not be used to accurately measure crack size through the layers of the FGM. Rather, crack size (a) was measured on the polished specimen surface using a traveling optical microscope after each crack extension increment. Cracks measured on the face of conventional metal specimens often do not give a reasonable representation due to the difference in crack size measured on the exterior (plane stress) compared to the crack size in the interior (plane strain) in ductile materials. Fortunately, however, the brittle Ti–TiB FGM material exhibits a relatively straight crack front with good correlation of the crack size at the face and center of the specimens as described in Reference 25. Tests were terminated after the cracks had propagated into the sixth layer in order to examine the interaction of the crack tip with TiB particles. The specimens were then heat-tinted at 400 °C in air for fifteen minutes to mark the end of crack growth, cooled to room temperature, and broken open.

Calculations of the elastic and plastic portions of the J-integral deviated from the ASTM E1820-20 standard due to the varying elastic modulus and Poisson's ratio. The elastic portion, J_{el}, was calculated from only the elastic properties of the FGM. As noted earlier, a significant plastic strain was expected near the crack tip in the most metallic layers of the FGM, thereby contributing a significant plastic component, J_{pl}. The latter was calculated using specimen geometry and the P-v_{pl} curve, where P is the load and v_{pl} is the plastic portion of the CMOD. However, ASTM E1820-20 is based on single input values for elastic modulus (E) and Poisson's ratio, which isn't appropriate for FGMs due to the variation in composition. Therefore, the J-integral calculations were modified to account for the change in modulus occurring at each interface, resulting in a piecewise calculation of J. In addition, because the shape of the J–a curve was non-standard (as shown below), it could not be used to calculate J_{Ic}.

To evaluate the above fracture parameters, it is necessary to know the values of elastic modulus and Poisson's ratio. In previous studies, these values were estimated from a nonlinear rule of mixtures calculation using a volume fraction interpolation that accounts for stress to strain transfer or measured by slicing small bilayer beams from the FGM and using strain gages to measure the modulus in bending.[14,25,26] To obtain more reliable elastic modulus values, nanoindentation was implemented in the present study consistent with the work of Cao, *et al.* and Constantinides, *et al.* on other FGMs.[27,28] A Nanomechanics iMicro with an InForce 1000 actuator was used along with a Berkovich indenter tip. Nanoindentation was performed using 500 mN of force and following the Oliver–Pharr method.[29] The FGM surface was indented roughly 1300 times with indents separated by 100 μm perpendicular to the layers and 100 μm parallel to the layers to ensure accuracy of the elastic modulus results of each layer. Determination of the modulus from nanoindentation also requires knowledge of Poisson's ratio (v) values, which were calculated from a linear rule of mixtures:

$$v = v_1 V_1 + v_2 V_2 \qquad [1]$$

Results for all indents within each layer were averaged to obtain elastic modulus values for each layer of the FGM.

III. RESULTS AND DISCUSSION

A. *Material Properties*

Table I presents the material compositions and widths of each layer of the FGM examined in the present study. Experimentally measured values of the elastic modulus from the nanoindentation tests are also listed in Table I along with values calculated from the modified rule of mixtures (modified RoM) that accounts for the nonlinear transfer of stress to strain in a composite that was used in previous work.[25,26,30] The values from the modified RoM reported here differ from those reported previously because updated elastic modulus values for TiB and CP Ti from the literature are used. The nanoindentation data are also displayed in Figure 2 to provide a visual representation of the results (with the first and last layers truncated for better interface resolution).

As shown in Figure 3, the nanoindentation modulus values of the FGM are in good agreement with those reported by Gooch, *et al.* from tensile and ultrasonic tests of individual specimens with varying ratios of Ti and TiB.[20] These results display only a very slight deviation from linearity. Values of modulus calculated from the modified RoM are also shown in Figure 3 and listed in Table I; they reflect a much stronger negative deviation from linearity. It is readily apparent that the modified RoM calculation significantly underestimates the modulus by as much as 28 pct, hence that approach is inappropriate for the nonlinear mechanical behavior and wide range of material variations exhibited by this FGM. Therefore, direct measurement of this property is preferred.
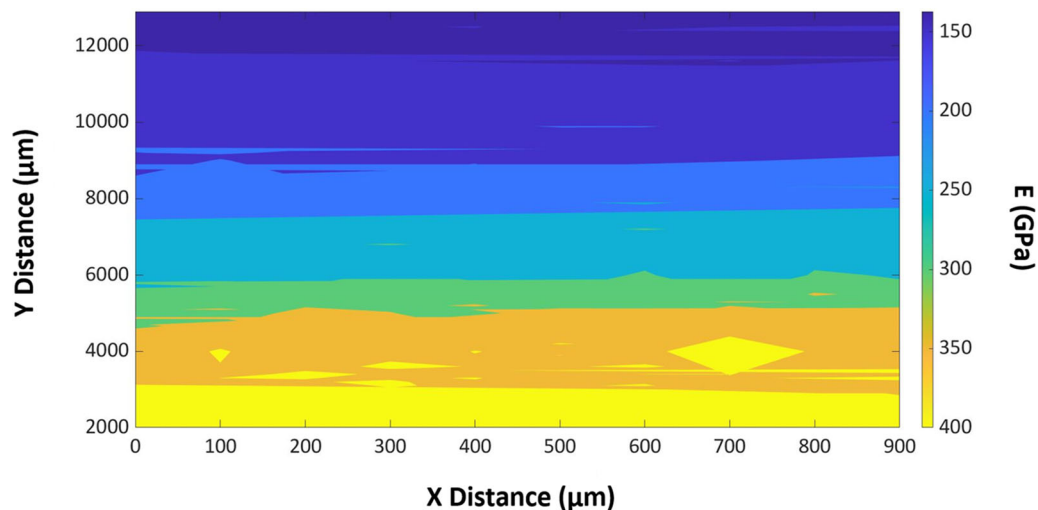

Fig. 2—Elastic modulus data acquired by nanoindentation of a Ti–TiB FGM, with the Ti layer at the top.
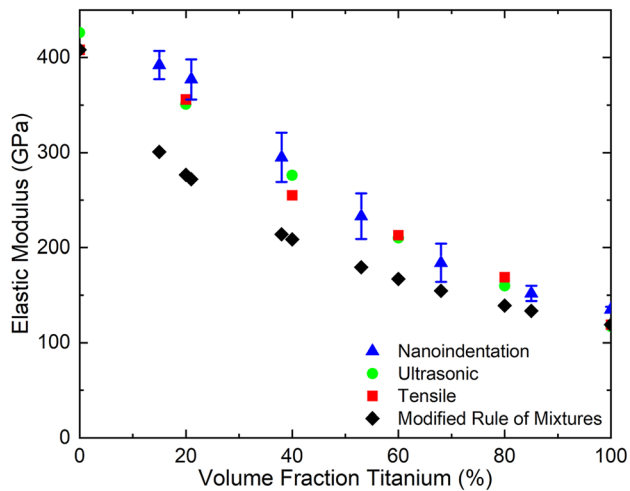
Fig. 3—Comparison of elastic modulus of Ti–TiB FGM acquired by various methods. Nanoindentation results were determined in this study while ultrasonic and tensile results were determined by Gooch, et al.[20].

Fig. 4—Plot of J_R vs Δa for three FGM specimens. Note that the results for FGM 6 correct previously published J_R values for that specimen[19] that were in error.

B. J-integral Calculation

To account for the changes in modulus within the interlayers for purposes of the J-integral calculation, the data for each specimen were divided into groups for each layer from 2 through 6 of the FGM. Calculations were then performed as described earlier in a manner consistent with ASTM E1820 for each group using the measured load, CMOD, crack size, and the specimen geometry, along with the experimentally determined values for elastic modulus and Poisson's ratio for each layer. The elastic and plastic portions of J were calculated, and their values were summed to obtain the total value of J_R. To visualize the fracture toughness of the FGM, a plot of J_R as a function of crack extension (Δa) was constructed and the results for three specimens are shown in Figure 4. The fact that the curves for specimens 4 and 6 are in excellent agreement provides verification that the results were reproducible when pre-cracking was accomplished using the reverse 4-point bending technique.[19] However, the J_R data for specimen 5a are slightly lower than those of specimens 4 and 6, most likely due to the fact that the latter were nearly adjacent to each other whereas the former came from a different region of the plate. Given the challenge of hot-pressing the FGM plate, it is not surprising to obtain different values in different regions. The R-curves presented in this paper also differ from the single curve presented in earlier work by Carpenter, et al.[19] and Paulino, et al.,[32] which were both determined from the same data using the modified RoM and a less precise fit of the measured values of load, crack size, and COD. Moreover, the previously reported R-curve was determined using an incorrect calculation of the elastic portion of J. The present results correct those prior shortcomings and provide additional data (instead of a single curve) to validate the measurements. It is apparent that the values of J are significantly lower than previously reported.
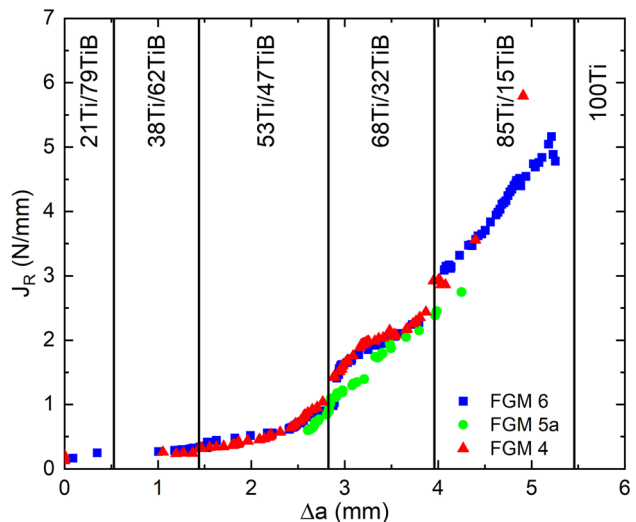
Figure 4 shows that the fracture toughness of the FGM increased as the crack grew from the ceramic-rich layers into the metal rich layers, thus confirming the rising R-curve behavior predicted by Jin and Batra.[33] However, the shape of the resistance curve is remarkably different from that obtained for a homogeneous material such as the CP Ti.[34] While both the FGM and CP Ti curves indicate rising R-curve behavior (with steps at the interfaces where the modulus and Poisson's ratio change in the former), the resistance to crack growth in the FGM is relatively low and constant as the crack travels through the ceramic-rich layers until the crack tip reaches layer 4 ($a \approx 1.4$ mm) at which point the resistance starts to increase at a more rapid rate. This is a direct result of the increased crack–particle interactions that occurred as the crack grew toward the metal rich layers as described in the next section. In comparison, the typical J–R curve for a ductile material such as CP Ti shows a rapid increase in crack growth resistance as the crack appears to extend but is actually blunted by the plastic deformation occurring at the crack tip. When the crack does start to grow, the slope of the curve decreases until it finally levels off during steady state crack growth. Previous studies have determined J_R of CP Ti to be 153 N/mm.[34] It should be noted that the present data show a dramatic decrease in fracture toughness from the CP Ti (layer 7) to 85 pct Ti/15 pct TiB (layer 6); with only 15 pct TiB added to the pure Ti, the fracture toughness decreases to roughly 5 N/mm—a value that is unacceptably low for engineering applications. This result is an indication of how rapidly the material changes from ductile to brittle with even a small addition of TiB. It also suggests that a different composition profile might be beneficial in a metal/ceramic FGM. Figure 5 illustrates the stepped changes in composition of this FGM and a linear fit from the first interface (layers 1 and 2) to the final interface (layers 6 and 7). This line indicates that this FGM has approximately a linear composition gradient. An
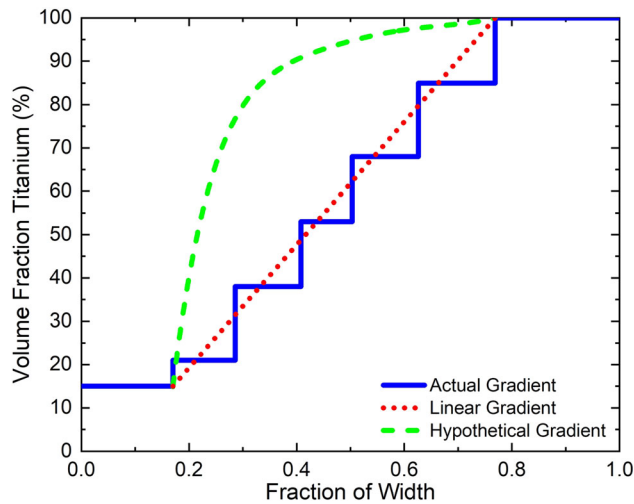
Fig. 5—Stepped composition gradient in the Ti–TiB FGM with a linear fit from first interface to last interface and a hypothetical polynomial composition profile.

alternative design strategy for metal/ceramic FGMs would be to increase the metal content more rapidly starting from the ceramic-rich side so that the final few layers have much higher metal content than the current material (85 pct Ti in the final layer prior to pure Ti). A hypothetical polynomial composition profile is shown by the dashed line in Figure 5. A similar nonlinear composition profile was explored computationally by Jin et al.[26] and Jin and Dodds.[30] However, the possible strategy of varying composition nonlinearly is not in agreement with the conclusion of Ravichandran that a linear composition gradient is preferred in order to minimize residual stress that may cause cracking in the FGM.[35]

C. Interactions of Cracks with TiB Particles

The SEM images of FGM 5a in Figures 6, 7(a), and 8 show a single primary crack progressing sequentially through layers 4, 5 and 6 respectively, to illustrate the interaction between the crack and the surrounding microstructure in the form of crack face bridging, crack-tip deflection, crack branching, and particle cracking as highlighted by the various circles and squares. Figure 7(b) illustrates the crack in layer 5 of a different specimen (FGM 5) and provides additional evidence that the aforementioned crack features represent a general observation. Interaction mechanisms such as these all lead to toughening because greater energy is needed to drive the crack through such obstacles. This toughening increases the measured J values compared to a rule of mixtures estimate.

The crack profile on the polished specimen face revealed a straight fracture typical of a brittle material exhibiting no interaction with TiB particles or deflection through layer 4 containing 53 pct Ti and 47 pct TiB as shown in Figure 6. The crack remained planar and orthogonal to the axis of applied stress. However, some Ti particle bridging of the crack behind the crack tip is evident. As the crack tip continued into layer 5
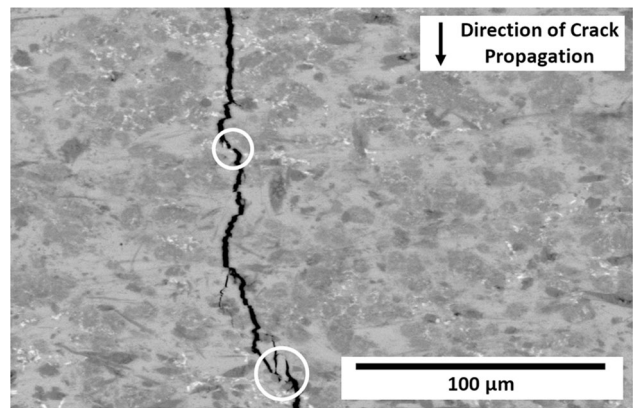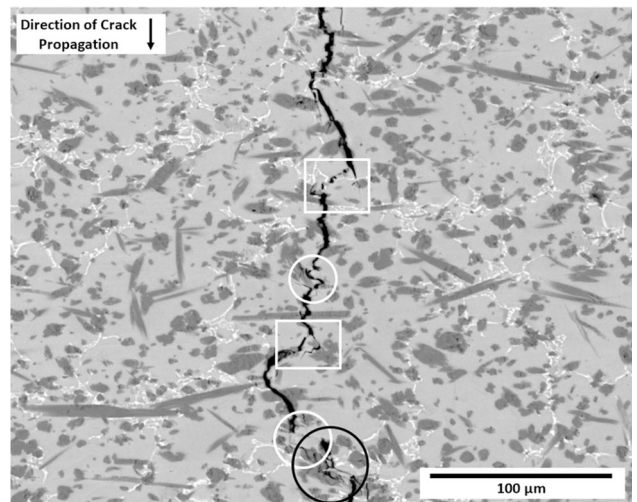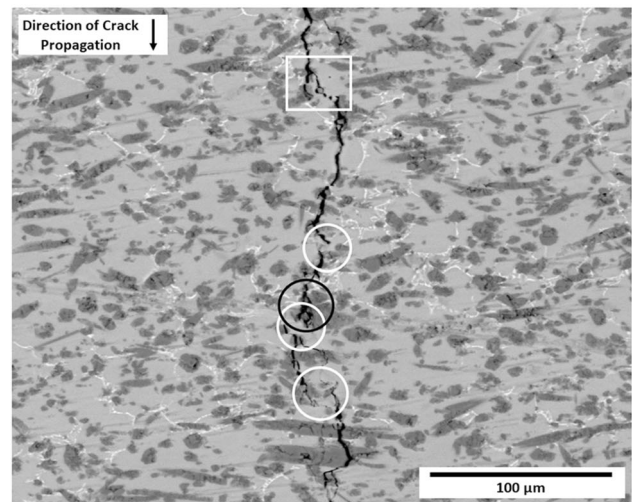

Fig. 6—SEM image showing crack face bridging (white circles) by Ti in FGM layer 4 (47 pct TiB).

(a)

(b)

Fig. 7—SEM images showing crack tip interaction with microstructural elements in FGM layer 5 (32 pct TiB) including cracking and debonding of the TiB particles (black circle), crack face bridging by the Ti matrix and TiB particles (white circles), and crack deflection (white boxes) in (a) FGM 5a and (b) FGM 5.
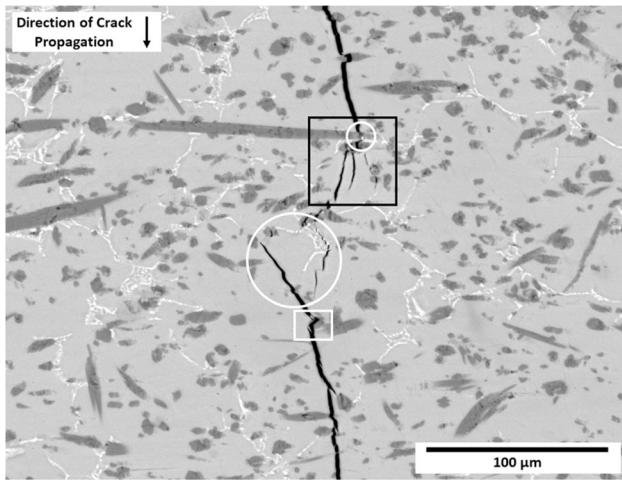
Fig. 8—SEM image showing crack tip interaction with microstructural elements in FGM layer 6 (15 pct TiB) including cracked and broken TiB particles. Crack branching (black box), crack deflection (white box), and crack bridging (white circles) are observed.
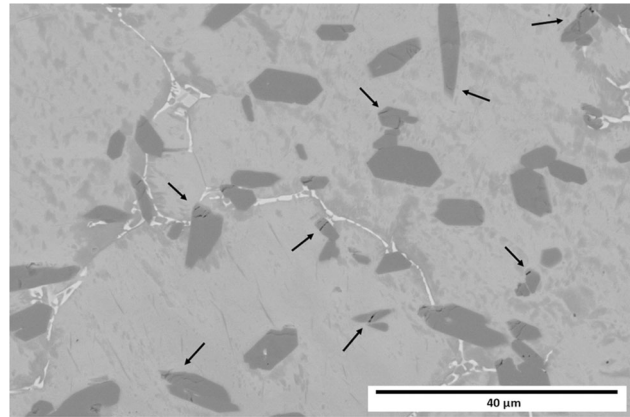

Fig. 9—SEM image of the as-received Ti–TiB FGM material showing microcracks (black arrows) in TiB particles in layer 6 (15 pct TiB). Local thermal stresses that developed during the cooling stage of the manufacturing process resulted in microcracks in the TiB particles.

containing 63 pct Ti and 37 pct TiB, the modest increase in ductility was sufficient to cause significant cracking and debonding of the TiB particles (Figure 7). As a consequence, crack propagation is affected by branching and bridging in the Ti matrix and re-nucleation leading to deflection of the crack tip. The crack tip region (Figure 8) reveals evidence of particle debonding from the matrix and particle fracture, reflecting the greater ductility of layer 6 compared to layer 5.

The crack path was strongly affected by the presence of TiB particles ahead of the crack tip. Many of the TiB particles fractured as the strain field around the crack tip encompassed them as is evident in Figures 7 and 8. The orientation of the cracked, needle type TiB particles was generally perpendicular to the crack growth direction, resulting in particle cracking and crack deflection as shown in Figure 7 for layer 5. Similar interactions were observed in layer 6 having 85 pct Ti and 15 pct TiB. The TiB needles in layer 6, however, were somewhat smaller than those in layer 5 and fewer exist per unit volume in layer 6 as visually determined from Figure 1. The ductility of layer 6 was larger than that of layer 5 and almost all of the TiB particles near the crack tip zone were cracked and debonded from the Ti matrix as shown in the SEM micrograph in Figure 8. The effect of these interaction mechanisms is consistent with the experimental rising *R*-curves in Figure 4, specifically for layers 5 and 6, where the brittle TiB particles are surrounded by a ductile Ti matrix. Finally, it is noted that the discontinuous NiTi phase does not seem to affect the crack path.

SEM examination of the as-received Ti–TiB FGM material revealed evidence of microcracking in the brittle TiB particles in layer 6 of the FGM as shown in Figure 9. As this figure shows, cracking occurred in both the blocky and the needle shaped TiB particles. Apparently, the local thermal stresses that developed during the cooling stage of the manufacturing process were large enough to crack some of the TiB particles.

Cracked particles such as these can actually have a twofold effect on increasing fracture toughness. In addition to reducing the driving force for crack growth at the crack tip, they can also serve as easy nucleation points for voids that can blunt the advancing crack tip.

Considering the overall interactions of the crack tips with the particles and matrix, relatively large crack deflections as well as crack branching were seen in the Ti–TiB FGM system. Figure 7 shows crack deflection that occurred in layer 5 of the Ti–TiB FGM, and Figure 8 shows crack branching in layer 6. The crack deflections and crack branching shown in this image were the result of the crack traveling preferentially around the more ductile Ti regions.

Crack face bridging was an operative mechanism in several layers of the Ti–TiB; representative examples are shown in Figures 6, 7, and 8. In Figure 6 the crack is bridged by ductile Ti fibers in the brittle layer 4 of the Ti–TiB FGM. In this case, the ductile phase, capable of plastic deformation, has elongated behind the crack tip producing crack closure tractions. This observation is consistent with the idea that microcracks nucleate ahead of the Ti grains as described in the previous section. Also, since additional energy is required to plastically deform or break the ligament behind the crack, less energy is available for crack propagation. Figure 8 shows crack face bridging by the brittle TiB particles in the more ductile layer 6. Here, the crack has passed around some particles and through others leaving large pieces of the particles in the crack wake. While crack face bridging is beneficial to enhancing toughness, the cracked particles also make a contribution. If the particles were broken by the crack as it passed, then that process absorbed energy and reduced the crack driving force. If the particles were already broken when the crack arrived in their vicinity, then the existing microcracks would serve to blunt the crack and distribute the applied stress. In either case, the bridging effect is enhanced by the presence of the broken particles.

IV. CONCLUSIONS

The results of this work represent a comprehensive experimental study of the fracture resistance and fracture mechanisms of a metal/ceramic FGM. An important purpose for developing the Ti–TiB FGM that was studied was to improve the room temperature fracture toughness of the brittle phase while retaining its good thermal resistance and hardness. The presence of the relatively ductile Ti phase allowed plastic deformation to occur ahead of the crack tip. Thus, the intrinsic toughness of the material system was increased by the presence of the second, ductile phase. In the Ti–TiB FGM, the distribution of the discrete, brittle TiB particles among the more ductile Ti phase allowed for plastic deformation of the matrix thereby increasing the energy absorbed by the system and increasing the resistance to crack propagation.

The specific microstructural toughening mechanisms in the FGM, including crack bridging by the Ti in the TiB-rich regions, crack deflection around TiB particles, and crack branching, resulted in the hypothesized rising R-curve behavior for the FGM beams. The unique increasing convex shape of the FGM R-curve can be attributed to the fracture toughness of the FGM increasing rapidly due to the changing composition gradient rather than solely to the state of the crack tip processes. This behavior is distinctly different from a ductile metal, for example, which displays an increasing concave R-curve due to crack blunting, crack growth initiation, and then steady-state crack growth.

Values of elastic modulus measured by nanoindentation in the present study revealed a nearly linear relationship between modulus and composition. This result indicates that the non-linear rule of mixtures previously used to estimate the elastic modulus in other investigations is not appropriate in this metal/ceramic FGM.

Finally, the results of the fracture tests of the Ti–TiB FGM system reveal that the toughness of the Ti decreases drastically, by 30-fold, with the addition of as little as 15 vol pct TiB to pure Ti. The very low toughness of even this layer is not suitable for engineering structures. Reproducible measurements of the modest increase of the J_R from less than 1 N/mm above 47 vol pct TiB to approximately 5 N/mm at 15 vol pct TiB indicates that lower volume fractions of TiB are needed on the metal-rich side to take advantage of the high toughness (153 N/mm) of the pure Ti. These results suggest the need to introduce layers of less than 15 vol pct TiB in the FGM. That is, it is possible that a nonlinear composition profile—in which the concentration of the ductile metal phase increases with distance at a rate greater than a linear relationship—might mitigate the dramatic decrease in toughness between adjacent layers and lead to improved fracture toughness of the FGM without compromising the desired ceramic phase properties.

DATA AVAILABILITY

Data are available upon request.

CONFLICT OF INTEREST

The authors declare no conflicts of interest in the work described herein.

REFERENCES

1. M. Niino, T. Hirai, and R. Watanabe: *J. Jpn. Soc. Compos. Mater.*, 1987, vol. 13(6), pp. 257–64.
2. M. Sasaki, Y. Wang, T. Hirano, and T. Hirai: *J. Ceram. Soc. Jpn.*, 1989, vol. 97(1125), pp. 539–43.
3. A. Kawasaki, R. Watanabe, Elsevier Science Pub. Co., Tokyo, Japan, 1987, pp. 1197–1202.
4. T. Fukushima, 1990, pp. 145–150.
5. Y. Miyamoto, H. Nakanishi, I. Tanaka, T. Okamoto, O. Yamada, Sendai, 1990, pp. 257–62.
6. N. Sata, N. Sanada, T. Hirano, M. Niino, in: Z.A. Munir, J.B. Holt (Eds.), VCH Publishers, New York, 1990, pp. 195–203.
7. A.P. Tomsia, E. Saiz, H. Ishibashi, M. Diaz, J. Requena, and J.S. Moya: *J. Eur. Ceram. Soc.*, 1998, vol. 18(9), pp. 1365–71.
8. J. Lambros, M.H. Santare, H. Li, and G.H. Sapna: *Exp. Mech.*, 1999, vol. 39(3), pp. 184–90.
9. D.R. Feenstra, R. Banerjee, H.L. Fraser, A. Huang, A. Molotnikov, and N. Birbilis: *Curr. Opin. Solid State Mater. Sci.*, 2021, vol. 25(4), p. 100924.
10. A. Reichardt, A.A. Shapiro, R. Otis, R.P. Dillon, J.P. Borgonia, B.W. McEnerney, P. Hosemann, and A.M. Beese: *Int. Mater. Rev.*, 2021, vol. 66(1), pp. 1–29.
11. Y. Li, Z.Y. Feng, L. Hao, L.J. Huang, C.X. Xin, Y.S. Wang, E. Bilotti, K. Essa, H. Zhang, Z. Li, F.F. Yan, and T. Peijs: *Adv. Mater. Technol.*, 2020, vol. 5(6), p. 1900981.
12. C. Zhang, F. Chen, Z.F. Huang, M.Y. Jia, G.Y. Chen, Y.Q. Ye, Y.J. Lin, W. Liu, B.Q. Chen, Q. Shen, L.M. Zhang, and E.J. Lavemia: *Mater. Sci. Eng. A*, 2019, vol. 764, p. 138209.
13. C.J. Han, Y. Li, Q. Wang, D.S. Cai, Q.S. Wei, L. Yang, S.F. Wen, J. Liu, and Y.S. Shi: *Mater. Design*, 2018, vol. 141, pp. 256–66.
14. M.R. Hill, R.D. Carpenter, G.H. Paulino, Z.A. Munir, and J.C. Gibeling: *Am. Soc. Test. Mater.*, 2002, vol. 1409, pp. 169–84.
15. Z.-H. Jin and R.C. Batra: *Int. J. Eng. Sci.*, 1996, vol. 34(15), pp. 1705–16.
16. Z.-H. Jin and R.C. Batra: *Mater. Sci. Eng. A*, 1998, vol. 242(1–2), pp. 70–76.
17. D.J. Shim, G.H. Paulino, and R.H. Dodds: *Int. J. Fracture.*, 2006, vol. 139(1), pp. 91–117.
18. D.P. Miller, J.J. Lannutti, and R.D. Noebe: *J. Mater. Res.*, 1993, vol. 8(8), pp. 2004–13.
19. R.D. Carpenter, G.H. Paulino, Z.A. Munir, and J.C. Gibeling: *Scripta Mater.*, 2000, vol. 43(6), pp. 547–52.
20. W.A. Gooch, B.H.C. Chen, M.S. Burkins, R. Palicka, J. Rubin, and R. Ravichandran: *Mater. Sci. Forum*, 1999, vol. 308, pp. 614–21.
21. S.S. Sahay, K.S. Ravichandran, R. Atri, B. Chen, and J. Rubin: *J. Mater. Res.*, 1999, vol. 14(11), pp. 4214–23.
22. K.B. Panda and K.S.R. Chandran: *Metall. Mater. Trans. A*, 2003, vol. 34A(9), pp. 1993–2003.
23. J.P. Quast, C.J. Boehlert, R. Gardner, E. Tuegel, and T. Wyen: *Mater. Sci. Eng. A*, 2008, vol. 497(1–2), pp. 1–9.
24. H.T. Tsang, C.G. Chao, and C.Y. Ma: *Scripta Mater.*, 1997, vol. 37(9), pp. 1359–65.
25. R.D. Carpenter, W.W. Liang, G.H. Paulino, J.C. Gibeling, and Z.A. Munir: *Mater. Sci. Forum*, 1999, vol. 308–311, pp. 837–42.
26. Z.-H. Jin, G.H. Paulino, and R.H. Dodds: *Eng. Fract. Mech.*, 2003, vol. 70(14), pp. 1885–1912.
27. G. Cao, L. Geng, and M. Naka: *J. Am. Ceram. Soc.*, 2006, vol. 89(12), pp. 3836–38.
28. G. Constantinides, K.S. Ravi Chandran, F.-J. Ulm, and K.J. Van Vliet: *Mater. Sci. Eng. A*, 2006, vol. 430(12), pp. 189–202.
29. W.C. Oliver and G.M. Pharr: *J. Mater. Res.*, 1992, vol. 7(6), pp. 1564–83.
30. Z.H. Jin and R.H. Dodds Jr.: *Eng. Fract. Mech.*, 2004, vol. 71(12), pp. 1651–72.
31. R.R. Atri, K.S. Ravichandran, and S.K. Jha: *Mater. Sci. Eng. A*, 1999, vol. 271(1–2), pp. 150–59.
32. G.H. Paulino, Z.-H. Jin, and R.H. Dodds: *Compr. Struct. Integr.*, 2003, vol. 2, pp. 607–44.
33. Z.-H. Jin and R.C. Batra: *J. Mech. Phys. Solids*, 1996, vol. 44(8), pp. 1221–35.
34. G.H. Paulino, R.D. Carpenter, W.W. Liang, Z.A. Munir, and J.C. Gibeling: *Eng. Fract. Mech.*, 2001, vol. 68(12), pp. 1417–32.
35. K.S. Ravichandran: *Mater. Sci. Eng. A*, 1995, vol. 201(1–2), pp. 269–76.